# Benchmark angle-differential cross-section ratios for the electron-impact excitation of the xenon $5p^6\ ^1S_0 \rightarrow 5p^5 6s[3/2]_2$, $5p^5 6s[3/2]_1$, $5p^5 6s'[1/2]_0$, and $5p^5 6s'[1/2]_1 + 5p^5 6p[1/2]_1$ transitions at low and near-threshold incident electron energies

A. Sakaamini,[1] J.-B. Faure,[1] M. A. Khakoo,[1,*] O. Zatsarinny,[2,†] and K. Bartschat[2]
[1]*Department of Physics, California State University, Fullerton, California 92831, USA*
[2]*Department of Physics and Astronomy, Drake University, Des Moines, Iowa 50311, USA*

(Received 17 October 2021; accepted 18 November 2021; published 10 December 2021)

Experimental benchmark intensity ratios for the angle-differential scattering intensities for electron-impact excitation from the xenon ground state $5p^6\ ^1S_0$ to its lowest five excited states $5p^5 6s[3/2]_2$, $5p^5 6s[3/2]_1$, $5p^5 6s'[1/2]_0$, and (combined) $5p^5 6s'[1/2]_1 + 5p^5 6p[1/2]_1$ are reported and compared to predictions from a full-relativistic *B*-spline *R*-matrix close-coupling model as well as earlier experimental work. The above ratios, which provide a stringent test of theoretical electron scattering models, are presented for this heavy rare gas with particular emphasis on the role of spin-exchange and direct excitation processes affecting their angular dependence.

DOI: 10.1103/PhysRevA.104.062805

## I. INTRODUCTION

The noble gases are interesting species as buffers in both industrial applications and atomic collision studies. Xenon is used in high-intensity discharge lamps [1], pulsed lamps [2,3], in lasers for medicine [3,4], in NMR studies of lungs [5], and other applications, for example, in plasma displays. It also has a rich target structure involving open shells in the excited states and is of particular interest in electron scattering involving spin-exchange and spin-orbit coupling relativistic effects, both in the target structure and for the scattering (continuum) projectile. Such processes are fundamental in electron-atom collisions. The inert rare gases are relatively easy to handle as targets for experimental electron-atom studies. As a consequence, they have been studied extensively, and much progress has been made in the theoretical modeling of electron–rare-gas collisions. Many of the advances in the theoretical modeling of collisions with them have subsequently been applied to other experimentally less inaccessible atomic targets, such as metals, halides, or other corrosive vapors.

It is, however, only recently that these major advances were made in the theoretical modeling, especially at low incident electron energies ($E_0$) in the threshold region near the low exited states and the ionization potential or slightly above. Presently, a paucity of data exist to challenge models in this near-threshold energy range. A survey paper on electron–rare-gas collisions (Ne, Ar, Kr, Xe) was written by Bartschat and Madison in 1987 [6]. Their calculations were based on the semirelativistic distorted-wave Born approximation (DWBA), which provides a perturbative solution to the electron-collision problem. In this model, exchange effects were approximately accounted for by a semiempirical (local) model potential along the lines of Furness and McCarthy [7], while the one-electron relativistic effects (most importantly the spin-orbit interaction) were also included. These potentials were added to the static Hartree potential of the final-state electron configuration of the target, and the distorted waves were calculated in the resulting potential. Their model did very well when compared, e.g., to the electron-photon coincidence work of Khakoo and McConkey [8] and measured differential cross sections (DCSs) for Ne, Ar, and Kr (see Ref. [6]).

This model was followed by a full-relativistic distorted-wave approximation (RDWA) [9], yielding comparable accuracy as the semirelativistic DWBA. In these models the rare-gas ground state $(np^6)\ ^1S_0$ and the excited $np^5(n+1)s$ states were described by just a single configuration each. The four excited states are combinations of *LS* states, two with total electronic angular momentum $J = 1$, the third with $J = 2$, and the fourth with $J = 0$. While the two states with total angular momenta $J = 0, 2$ are well *LS* coupled, the $J = 1$ states are a linear combination of two states, with the details depending on the coupling scheme used. A popular scheme is the so-called intermediate coupling adopted by Cowan [10], in which a linear combination of *LS*-coupled $^1P_1$ and $^3P_1$ states is used to describe these excited $np^5(n+1)s$ $(J = 1)$ states of the rare gases. One can, of course, extend this to a multiconfiguration expansion framework using higher-lying *LS* states as well. For example, a multiconfiguration expansion (eight or more terms) for the $2p^5\ 3s$ states of Ne was used in [11].

Major breakthroughs came in the 1990s. As a result of increasing computational power, physically more accurate close-coupling methods began to do much better than perturbative theories, especially at near-threshold energies for excitation of relatively simple quasi-one- and quasi-two-electron targets, such as atomic hydrogen and helium as well as the light alkalis and alkaline earth atoms. These were

*mkhakoo@fullerton.edu
†Deceased.

 

the convergent close-coupling (CCC) [12,13] and *R*-matrix (close-coupling) with pseudostates (RMPS) [14,15] methods. The use of pseudostates extended the traditional low-energy close-coupling method to intermediate and (possibly) high energies. Pseudostates have the mathematical properties of bound states. Most importantly, they are easily normalizable, but due to their confinement to either a hard (*R* matrix) or a soft (CCC with a Laguerre basis) box, they provide a proper discretization of the target continuum. While these methods have been extremely successful for light (quasi-) one-electron and (quasi-) two-electron atomic and ionic targets, even (recently) for the $H_2$ molecule [16], the situation is much less satisfactory for more complex, open-shell targets. The challenges are increased if these targets are also heavy, because both electron-electron correlation and relativistic effects need to be described properly by the theoretical methods.

The currently available CCC models are generally limited to one-electron [12,17] and two-electron systems [18] outside of a structureless $^1S_0$ or $^1\Sigma_0$ core [19]. In these cases the resulting collision data are impressively accurate and benchmark cross sections for electron scattering from such targets have been generated. This success clearly revealed that close-coupling calculations provide the most physically tractable and accurate method for solving low-energy electron-atom or electron-molecule scattering problems, as was suggested early on by Poet [20] for atomic hydrogen in a simplified *S*-wave model. The well-known *R*-matrix close-coupling model of the Belfast group [21] was demonstrated for more complex targets with relativistic effects [22]. However, numerous high-quality experimental datasets (see, e.g., Refs. [23–26] from our group) continued to represent significant challenges to theoretical treatments of the heavy rare gases (Kr, Xe), leading theoreticians to seek further progress in developing sophisticated approaches and the associated computer codes for electron collisions with complex targets.

A very promising method available for these rare-gas targets is the recent *B*-spline *R*-matrix (BSR) approach that allows the use of nonorthogonal sets of one-electron orbitals, employing *B* splines to represent them. Technically, this has the advantages of compact configuration-interaction expansions to yield sufficient accuracy as well as the availability of accurate and efficient integration schemes. A general computer code that can be used for calculations of atomic structure, photo-ionization, and electron collisions in a nonrelativistic and semirelativistic (Breit-Pauli) framework was published by Zatsarinny [27] and has been used for numerous calculations of the above processes. For a general overview of the method and its applications until 2013 we refer to the review by Zatsarinny and Bartschat [28]. Similar to the Belfast code, the available suite of computer codes is general; i.e., it is applicable to targets such as the heavy noble gases of interest for the present work. A fully relativistic version described by Zatsarinny and Bartschat [29] also exists. While a comprehensive write-up is not presently available due to the recent passing of Dr. Zatsarinny in March 2021, the BSR code with instructions is freely available from his GitHub site [30]. Furthermore, attempts to make the code accessible to a wider audience, i.e., not just specialists, is currently being undertaken on the Atomic, Molecular, and Optical Science (AMOS) Gateway [31].

## II. ANGLE-DIFFERENTIAL CROSS-SECTION RATIOS

In the past, for the rare gases, there were significant disagreements observed between theory and experiment, for angle-differential and even angle-integrated cross sections. These were usually accredited to problems in the absolute normalization process of the experimental data using conventional electrostatic electron spectrometers [32]. This problem is difficult to overcome systematically when normalizing inelastic scattering features, with nonzero energy loss $E_L$, to the elastic standard scattering feature ($E_L = 0$) in an energy loss spectrum acquired by the electrostatic spectrometer. This needs a reliable and accurate characterization of the spectrometer's analyzer's detection efficiency for different $E_L$ values in the energy loss spectrum. Here, in order to obtain absolute inelastic DCSs, the scattering intensities of inelastic features in the same energy loss spectrum are normalized to the elastic scattering intensity by using DCSs for elastic scattering at the same $E_0$ and scattering angle $\theta$. This requires that the analyzer's detection efficiency characterized by the residual electron energy $E_R(= E_0–E_L)$ is accurately known. Standardized elastic scattering DCSs are accurately determined by using the well-established relative flow method [33] in the ≈10% uncertainty region. Knowing an accurate analyzer detection efficiency characteristic, the absolute inelastic DCSs may be determined from the spectrum, provided the elastic DCS is known in tandem with the analyzer detection efficiency.

This is indeed the case for electron time-of-flight (TOF) electron spectrometers, where—unlike for conventional electrostatic spectrometers—the detection efficiency is independent of $E_R$ of the scattered electron, since the system does not employ electrostatic focusing in the electron detector. In our laboratory, we recently built an electron time-of-flight (TOF) spectrometer to determine such accurate elastic-to-inelastic differential electron scattering *ratios* for the excitation of the $H_2$ $X\,^1\Sigma_g^+ \rightarrow b\,^3\Sigma_u^+$ transition [34]. These benchmark ratios (which were measured by the TOF system) were found to be in excellent agreement with predictions from the CCC model by the Curtin University group [34]. After normalizing our TOF spectrum's elastic feature to well-established elastic electron scattering DCSs from our group [35], we determined benchmark experimental DCSs for elastic and inelastic processes for the $H_2$ molecule and again found excellent agreement with the CCC [34].

Inelastic scattering ratio measurements had been carried out by us earlier for Ne [11], Kr [25], and Xe [23]. DWBA calculations for these ratios were reported by Bartschat and Madison [36], with particular emphasis on observed deviations from statistical weight ratios. Referring to the excellent agreement between the experimental ratios in [11] and the predictions from their semirelativistic BSR calculations for Ne, Zatsarinny and Bartschat [37] commented that such DCS ratios in the noble gases are "a very sensitive test to the quality of the theoretical model." Finding that it is easier and more accurate to measure relative ratios in scattering experiments,

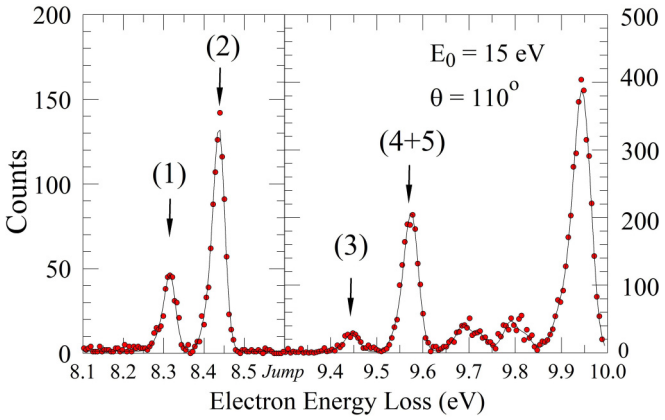


FIG. 1. Electron energy loss spectrum of Xe taken at $E_0 = 15.0\,\text{eV}$ and $\theta = 110^\circ$. (•) data; (—) linear least-squares fit to the spectrum using a multi-Gaussian instrumental line profile centered at the empirical $E_L$ values given by Moore [41], also listed in Table II. The features $m = 1, 2, 3$, and 4+5 are discussed in the text following Eqs. (1)–(4) and are also listed in Table I.

we recently decided to revisit inelastic scattering ratios for the lowest transitions in Kr [38] and provided experimental benchmark data for testing an existing BSR model for Kr [39]. This model had been employed to calculate benchmark DCSs for the electron-impact excitation of the individual electronic states in the $4p^6\ {}^1S_0 \rightarrow 4p^5 5s$ transitions. Our significantly improved results in tandem with earlier measurements of these ratios [25] showed very good to excellent agreement with a 31-state model for the excitations in Kr and provided great encouragement on the theoretical progress of the BSR concerning the situation for electron-impact excitation in the rare gases. We also pointed out areas where theory needed small improvements.

The present work is similar to [38], but is carried out on the corresponding transitions in Xe to draw attention to such ratios as benchmarks to aid theory in the critical area of experimental and theoretical electron-collision physics for Xe, which is even more challenging than Kr due to the increased nuclear charge and the particular level structure. Unlike in Kr, we could not resolve the $5p^6\ {}^1S_0 \rightarrow 5p^5 6s'[1/2]_1$ excitation from the neighboring $5p^5 6p[1/2]_1$ excitation (see Fig. 1). Hence our definition of the ratios in Eqs. (2) and (4) below differs somewhat from similar ratios in Kr. In the present paper, we define these ratios as follows:

$$r(E_0,\theta) = \frac{\sigma(6s[3/2]_2)}{\sigma(6s'[1/2]_0)}, \tag{1}$$

$$r'^{(E_0,\theta)} = \frac{I_2(E_0,\theta)}{I_{4+5}(E_0,\theta)} = \frac{\sigma(6s[3/2]_1)}{\sigma(6s'[1/2]_1) + \sigma(6p[1/2]_1)}, \tag{2}$$

$$r''^{(E_0,\theta)} = \frac{I_1(E_0,\theta)}{I_2(E_0,\theta)} = \frac{\sigma(6s[3/2]_2)}{\sigma(6s[3/2]_1)}, \tag{3}$$

and

$$r'''^{(E_0,\theta)} = \frac{I_3(E_0,\theta)}{I_{4+5}(E_0,\theta)} = \frac{\sigma(6s'[1/2]_0)}{\sigma(6s'[1/2]_1) + \sigma(6p[1/2]_1)}. \tag{4}$$

Here, $I_m\ (E_0,\theta)$ are the intensities of the electron energy loss features for excitation of the $m = 1$ to 4 (see labels in Fig. 1) for the $5p^6\ {}^1S_0 \rightarrow 5p^5 6s$, $6s'[K]_J$ transitions, and $m = 5$, in (Fig. 1) for the $5p^6\ {}^1S_0 \rightarrow 5p^5 6p[1/2]_1$ transition, which could not be resolved from the nearest-lying $5p^6\ {}^1S_0 \rightarrow 5p^5 6s'[1/2]_1$ $m = 4$ feature. These intensities are proportional to their corresponding DCSs ($\sigma$). In the notation and discussion below, we use the intermediate-coupling scheme [10,11] that is appropriate for the heavy noble gases, where $K$ is the total angular momentum of the parent ion ($Xe^+$) $5p^5$ core and $J$ is the total angular momentum of the core plus the valence $6s$, $6s'$, or $6p$ electron. Table I shows the result of a multiconfiguration expansion of the states of interest in this work. The Cowan code [10] only uses term-averaged $6s$ and $6p$ orbitals. One can clearly see for the excited levels 1–3 that a single configuration dominates in all cases, but for levels 4 and 5 more than one configuration is involved significantly. Based on Table I, the $J = 1$ states are approximately $a \approx 60/40$ mix of states with dominant $5p^5 6s$ singlet and triplet character, except that the $6s'[1/2]_1$ state includes a small (≈10% after squaring the coefficient) contribution from the $5p^5 5d\ {}^3P_1$ configuration.

The ratio $r$ defined in Eq. (1) addresses the ratio between the pure triplet $6s[3/2]_2(^3P_2)$ and $6s'[1/2]_0(^3P_0)$ states (with its approximate $LS$-coupled component in brackets), respectively. Since the statistical weights of these states are $2J + 1$, one would expect the DCS ratio to be close to 5 for a well $LS$-coupled system, provided one can neglect the energy difference between the two states as well as the potential term

TABLE I. Intermediate-coupling coefficients for the $5p^6$ and $5p^5 6s$, $5p^5 6s'$, and $5p^5 6p$ states of Xe in a multiconfiguration expansion, obtained with the Cowan code [10] by Fontes [40]. $E_L$ values from the Cowan code and from Moore [41] are also displayed. The notation $[K]_J$ (see text) indicates the total electronic angular momentum of the $(5p^5)^2P_K$ ionic core. After coupling to the outer electron orbital (here $6s$ or $6p$ or $5d$), this results in a total angular momentum $J$ of the state. See text for more discussion.

| Level number | Configuration | Intermediate coupling | Energy (eV) Cowan [10] | Energy (eV) Moore [41] |
|---|---|---|---|---|
| **0** | $5p^6\ {}^1S_0$ | $0.998\ ((5p^6\,{}^1S_0) + \cdots$ | 0 | 0 |
| **1** | $6s[3/2]_2$ | $0.996\ (5p^5 6s\,{}^3P_2) + \cdots$ | 8.361 | 8.315 |
| **2** | $6s[3/2]_1$ | $0.777\ (5p^5 6s\,{}^1P_2) + 0.626(5p^5 6s\,{}^3P_1) + \cdots$ | 8.458 | 8.437 |
| **3** | $6s'[1/2]_0$ | $0.906\ (5p^5 6s\,{}^3P_0) + 0.413(5p^5 5s\,{}^3P_0) + \cdots$ | 9.537 | 9.447 |
| **4** | $6s'[1/2]_1$ | $0.72\ (5p^5 6s\,{}^3P_1)$–$0.61(5p^5 6s\,{}^1P_1) + 0.33(5p^5 5d\,{}^3P_1) + \cdots$ | 9.618 | 9.570 |
| **5** | $6p[1/2]_1$ | $0.86(5p^5 6p\,{}^3S_1)$–$0.46(5p^5 6p\,{}^3P_1) + 0.21(5p^5 6p\,{}^1P_1) + \cdots$ | 9.577 | 9.580 |

dependence of the valence orbital. In order to indicate those possible effects, we follow the standard notation of using $6s$ and $6s'$ $6s'$ for the outer orbital when the parent ion is either the $(5p^5)^2P_{3/2}$ (for $6s$) or the $(5p^5)^2P_{1/2}$ (for $6s'$) core state. On the other hand, the ratio $r'$ defined in Eq. (2) addresses the ratio between the $6s[3/2]_1$ and $6s'[1/2]_1 + 6p[1/2]_1$ states. Unlike the situation in Kr, here the $6s'[1/2]_1$ excitation (level 4, Table I) is not resolved from the $6p[1/2]_1$ excitation (level 5, Table I) and the arguments regarding the dipole limit of the $r'$ that could be applied in our Kr experiment [38] are not applicable here for Xe. Nevertheless, $r'$ still supplies a useful quantitative test of theory here regarding these states.

Next, $r''$ defined in Eq. (3) represents the ratio of the $LS$-coupled $6s[3/2]_2$ ($^3P_2$) state and the mixed-coupled $6s[3/2]_1$ state, while $r'''$ defined in Eq. (4), in a similar fashion as $r''$, is the ratio between the pure $6s'[1/2]_0$ ($^3P_0$) state and the other mixed state $6s'[1/2]_1 + 6p[1/2]_1$. From an experimental point of view, it is important to note that both $r''$ and $r'''$ are less affected by the instrumental transmission efficiency than $r$ and $r'$, since the features in $r''$ and $r'''$ are very closely spaced in $E_L$; i.e., they have almost equal $E_R$ values that control the scattered electron detection efficiency. This is especially important at low $E_0$ values close to threshold and will be further addressed in the experimental section below.

In this work, the recently obtained inelastic DCS ratios for Xe are presented in comparison with the respective theoretical predictions, as well as the earlier Xe experimental ratios obtained in our group by Khakoo *et al.* [23] and ratios determined from the DCSs in the earlier work of Filipović *et al.* [42] who also measured similar DCSs for features 1, 2, 3, and 4+5 (see Fig. 1), but at higher $E_0$ values of 15, 20, 30, and 80 eV with $\theta$ from 5 ° to 150 ° and extrapolated DCSs for $\theta = 0°$. A summary of the full-relativistic D(irac)BSR (DBSR) electron scattering model for Xe is given in Sec. III. More details of the theory, for both Kr and Xe, can be found in [39]. A discussion of the experimental apparatus and the measurement procedures for obtaining the above-mentioned DCS ratios is given in Sec. IV. The experimental and theoretical results are presented and discussed in detail in Sec. V followed by conclusions in Sec. VI.

## III. THEORY

Because the details of the calculation were given by Zatsarinny and Bartschat [39], we only summarize the main points here. The calculations reported in this paper were performed using the $R$-matrix (close-coupling) approach, as implemented in the DBSR suites of computer codes. The initial structure calculation for $Xe^+$, similarly to $Kr^+$ [39], was carried out with the GRASP2K relativistic atomic-structure package [43]. After that the valence orbitals were generated in a frozen-core calculation for $Xe^+$, employing the average-term approximation. All these states of $Xe^+$ were then used as target states in $B$-spline bound-state close-coupling calculations to generate the low-lying states of atomic Xe (with $N = 54$ electrons) employing nonorthogonal, term-dependent orbitals for each state.

In the scattering calculations, we included (similarly to Kr) the lowest 31 physical states of Xe, i.e., the fine-structure levels with configurations $5p^56s$, $5p^56p$, $5p^55d$, and $5p^57s$, respectively. This model will be referred to as DBSR-31 below. Since this is a full-relativistic approach, the mixing coefficients in the multiconfiguration expansions are mathematically not the same as in the intermediate-coupling scheme. This is a similar situation as in the RDW model [9]. In a truly complete expansion, the specifics of the numerical basis would not matter. While this ideal situation is not achievable in practice, it still makes some sense to interpret the final results in the intermediate-coupling scheme, which appears to capture the essential physics regarding the orbital and spin angular-momentum character of the states in question.

We then used the DBSR version [29] to solve the $(N + 1)$-electron-collision problem. We calculated partial-wave contributions up to $J = 61/2$ numerically. No extrapolation scheme to account for even higher partial waves was necessary for all observables presented in this paper.

At this time, only results from the 31-state model are available. In the original paper [39], 75-state results were also presented, but the calculations were limited to energies below 10.5 eV. Note that the general features seen in the near-threshold region were reproduced in both models and the DBSR-31 and DBSR-75 predictions were often very similar. Ideally, one would extend the present calculations much further to include an even larger number of physical and pseudostates, i.e., to also couple to the ionization continuum. Due to the passing of Dr. Zatsarinny, however, this is presently not possible, but such calculations are planned for the future.

## IV. EXPERIMENT

The present California State University (CSUF) energy loss system is a moderate current, high-resolution electrostatic energy loss spectrometer, which has been well tested and described in detail before [44]. The system consists of an electron monochromator and an electron energy analyzer, with both employing double hemispherical energy selectors. The collimated gas beam is delivered to the collision region via a movable gas thin aperture source, which is aligned and placed about 5 mm below the collision region. The entire spectrometer is housed in a magnetically shielded vacuum chamber that is pumped with a 12 in. diameter diffusion pump down to a base pressure of $\approx 1 \times 10^{-7}$ Torr. In order to create and maintain an environment suitable for measuring stable low-energy electron energy loss spectra over long periods of time, the electron gun and energy analyzer are both baked to about 120 °C during the experiment, and the vacuum chamber is properly oil baffled with a low-temperature Freon trap.

The experimental apparatus is computer controlled via the LABVIEW program. The latter is run in the multichannel scaling mode and monitors the input pressure of the target gas, steers the movable gas source in and out of the interaction region, drives a stepper motor that sets the scattering angle position of the electron energy analyzer, and controls the energy loss ramp of the electron energy analyzer. The experimental energy loss spectra acquired by the multichannel scaling program are analyzed by separate software that employs a multi-Gaussian instrumental line-profile unfolding technique to fit the energy loss spectra [44].

Xenon energy loss spectra (e.g., Fig. 1) were acquired for $E_0$ values of 9.5, 10.0, 12.5, 15.0, 17.5, and 20.0 eV for $\theta$

TABLE II. Transmission parameters that affect the ratios $r$, $r'$, $r''$, and $r'''$. The $E_L$ values, listed in increasing order for the $6s[3/2]_2$, $6s[3/2]_1$, $6s'[1/2]_0$, and $6s'[1/2]_1$ states, are taken from the recommended values of Moore [41]. See text for a detailed discussion.

| $E_0$(eV) → | 9.5 | 10 | 12.5 | 15 | 17.5 | 20 |
|---|---|---|---|---|---|---|
| $E_L$ (eV) | | | $E_R$ (eV) | | | |
| 8.315 | 1.185 | 1.685 | 4.185 | 6.685 | 9.185 | 11.685 |
| 8.437 | 1.063 | 1.563 | 4.063 | 6.563 | 9.063 | 11.563 |
| 9.447 | 0.053 | 0.553 | 3.053 | 5.553 | 8.053 | 10.553 |
| 9.575 | – | 0.425 | 2.925 | 5.425 | 7.925 | 10.425 |
| | | | $\Delta E_R/E_{R\,\mathrm{bar}}$ | | | |
| $r$ | 1.83 | 1.01 | 0.313 | 0.185 | 0.131 | 0.102 |
| $r'$ | – | 1.14 | 0.326 | 0.190 | 0.134 | 0.104 |
| $r''$ | 0.0271 | 0.0188 | 0.0074 | 0.0046 | 0.0033 | 0.0026 |
| $r'''$ | – | 0.0654 | 0.0107 | 0.0058 | 0.0040 | 0.0031 |

ranging from 10 ° to 120 ° with a typical energy resolution of ≈ 35–45 meV for an incident current of ≈ 13–22 nA. The electron beam $E_0$ was calibrated using the $He^-(1s2s^2)^2S$ resonance at 19.366 eV at $\theta = 90°$ [45,46] to obtain $E_0$ with an accuracy of 50 meV or better during the entire run at a fixed $E_0$ value. The CSUF spectrometer and the earlier spectrometer at the NASA–Jet Propulsion Laboratory, Pasadena, California (JPL) in [23] differ somewhat, in that the former used real apertures in the analyzer as opposed to virtual apertures in the CSUF spectrometer. Additionally, the CSUF spectrometer employed a thin aperture gas-target collimation system rather than the earlier JPL hypodermic needle gas collimator. In this experiment, the movable gas source was kept fixed, because the system was not observing elastic scattering as it did in previous work [47] where elastic background scattering from surfaces was found to be significant. This also improved the acquired scattering counts (more acquisition time for inelastic measurements with the gas beam aligned with the electron beam) and thus reduced the statistical uncertainties.

An important consideration in this experiment was to control the transmission efficiency for the different features (features 1, 2, 3, and 4+5 in Fig. 1), which had respective $E_L$ values of 8.315, 8.437, 9.447, and 10.575 ≈ [10.570+10.580]/2 eV. At small $E_0$ values, the $E_R$ of the scattered electrons becomes significantly different across the energy loss spectrum.

Since the transmission efficiency of the electron detector is dependent on $E_R$ it can significantly vary for the different inelastic features. Table II shows the ratio $\frac{\Delta E_R}{\overline{E_R}}$ $(= \alpha)$ at different $E_0$ values for the four ratios, where, e.g., in the case of $r$, features 1 and 3, $\Delta E_R = E_R(1)$–$E_R(3)$ is the difference between the residual energies of scattered electrons exhibiting features 1 and 3, and $\overline{E_R} = [E_R(1) + E_R(3)]/2$ is the mean residual energy of these features. Assuming that the transmission efficiency is approximately a linear function across the spectrum vs $E_R$, $\alpha$ gives the value of the fractional difference in the transmission of electrons for the features involved. At $E_0 = 12.5$ eV, for example, $r$ and $r'$ have relative fractional transmission differences of ≈32% while those of $r''$ and $r'''$ are only ≈1%. This means that the measured ratios $r''$ and $r'''$ are much more precise as benchmarks than $r$ and $r'$.

In order to control this transmission problem, the scattered electron detector analyzer was first tuned to the average mid–residual energy of features 1 and 3 or 2 and 4, which are similar for both $r$ and $r'$ at any $E_0$ value. For example, at $E_0$ for features 1 and 3 ($r$) the mid–residual energy is 3.619 eV = [4.185 + 3.053]/2) eV and for features 2 and 4 ($r'$) it is 3.474 eV = [4.063 + 2.925]/2 eV (see Table II). This required tuning the gun and analyzer to the elastic scattering at 90 ° at $E_0 = \overline{E_R}$ (e.g., at $E_0 = 12.5$ eV, $\overline{E_R} \approx 3.55$ eV). Furthermore, the electron gun would be set to this $E_0 = \overline{E_R}$ value of 3.55 eV and the analyzer maximized for elastic scattering. The electron gun was then retuned to deliver a focused beam at the $E_0$ of the required value (in this case 12.5 eV). As a result, the transmission peaked at approximately the mid-$E_L$ of states 1 and 3 or 2 and 4, while it fell equally at $E_L$ values of the features on either side of this maximum, thus giving consistently reproducible and accurate $r$ and $r'$ values by breaking away from a skewed transmission function for the $r$ and $r'$ features. This procedure does not affect $r''$ and $r'''$, which were always well reproduced for any tuning conditions of the analyzer. At $E_0 = 15$ eV, this problem is diminished, and the $r$ and $r'$ ratios were found to be reproducible with ≈11% uncertainties.

## V. RESULTS AND DISCUSSION

Parts (a–f) of Table III list the ratios $r$, $r'$, $r''$, and $r'''$ at different $E_0$ values as a function of $\theta$. Figures 2–5 display these ratios from the current measurements along with the previous ratios of [23,42] and the DBSR-31 results. Our estimated errors for all ratios of [42] are ±15%, since the authors did not rigorously account for the likely change in transmission efficiency between features 1 to 4+5. We also note that the $\theta = 0°$ data of [42] are extrapolated results.

Figure 2 exhibits $r$ ratios at several $E_0$ compared to our previous measurements [23] and the DBSR-31 theory. Unlike in the recent similar work with Kr [38], where we observed excellent agreement for all $E_0$ values with our earlier $r$ values, as well as with the DBSR-31 predictions, we see less agreement here for Xe. For example, at $E_0 = 12.5$ eV, there is somewhat qualitative agreement, but significant disagreement of up to 50% with theory. At $E_0 = 15$ eV, we see good agreement between the present measurements and [23] for $\theta \geqslant 40°$, and $\theta \geqslant 90°$ between the present measurements and [23,42], but the DBSR-31 model does not reproduce the angular dependence, showing a "bump" at $\theta \approx 110°$ that is not seen in any of the experimental datasets.

Based on the experimental errors and the agreement between the three experiments, this bump is about five standard deviations of the error bars outside of the present experimental results and about three standard deviations away from the other experiments [23,42]. This suggests a problem with the theory. At $E_0 = 17.5$ eV, the present work shows good agreement with the DBSR model across the complete angular range. At $E_0 = 20.0$ eV, the present experiment and [23] agree very well for $\theta \leqslant 100°$, but we note again disagreement with theory, especially at forward scattering angles and $\theta \approx 70°$–$80°$, where the predictions are about 50% below the experimental $r$ ratios. The $r$ values of [42] trend significantly

TABLE III. Angle-differential $r$, $r'$, $r''$, and $r'''$ values with associated errors taken at (a) $E_0 = 9.5\,\text{eV}$, (b) $E_0 = 10.0\,\text{eV}$, (c) $E_0 = 12.5\,\text{eV}$ (d), $E_0 = 15.0\,\text{eV}$ (e) $E_0 = 17.5\,\text{eV}$, and (f) $E_0 = 20.0\,\text{eV}$. See text for discussion.

| (a) $\theta$ (deg) | $r''$ | Error |
|---|---|---|
| 20 | 0.357 | 0.030 |
| 25 | 0.326 | 0.024 |
| 30 | 0.278 | 0.021 |
| 35 | 0.320 | 0.023 |
| 40 | 0.360 | 0.026 |
| 45 | 0.424 | 0.032 |
| 50 | 0.565 | 0.041 |
| 60 | 0.972 | 0.089 |
| 70 | 1.57 | 0.14 |
| 80 | 1.86 | 0.25 |
| 90 | 1.76 | 0.24 |
| 100 | 1.13 | 0.11 |
| 110 | 0.627 | 0.047 |
| 120 | 0.383 | 0.029 |

| (b) $\theta$ (deg) | $r''$ | Error |
|---|---|---|
| 20 | 0.673 | 0.059 |
| 25 | 0.773 | 0.068 |
| 30 | 0.762 | 0.067 |
| 35 | 0.674 | 0.049 |
| 40 | 0.736 | 0.051 |
| 45 | 0.707 | 0.049 |
| 50 | 0.600 | 0.045 |
| 60 | 0.578 | 0.041 |
| 70 | 0.525 | 0.039 |
| 80 | 0.543 | 0.039 |
| 90 | 0.608 | 0.049 |
| 100 | 0.578 | 0.041 |
| 110 | 0.583 | 0.042 |
| 120 | 0.539 | 0.037 |

| (c) $\theta$ (deg) | $r$ | Error | $r'$ | Error | $r''$ | Error | $r'''$ | Error |
|---|---|---|---|---|---|---|---|---|
| 20 | 7.55 | 0.97 | 2.71 | 0.25 | 0.128 | 0.023 | 0.068 | 0.028 |
| 25 | 7.40 | 0.74 | 2.02 | 0.35 | 0479 | 0.055 | 0.122 | 0.018 |
| 30 | 7.21 | 0.70 | 2.18 | 0.20 | 0.576 | 0.051 | 0.175 | 0.025 |
| 35 | 5.79 | 0.67 | 2.43 | 0.21 | 0.494 | 0.052 | 0.162 | 0.015 |
| 40 | 5.90 | 0.60 | 2.38 | 0.25 | 0.412 | 0.034 | 0.166 | 0.018 |
| 45 | 4.22 | 0.46 | 2.25 | 0.33 | 0.348 | 0.031 | 0.185 | 0.019 |
| 50 | 4.62 | 0.69 | 1.77 | 0.16 | 0.396 | 0.063 | 0.151 | 0.008 |
| 60 | 4.23 | 0.47 | 1.50 | 0.20 | 0.387 | 0.058 | 0.137 | 0.012 |
| 70 | 4.15 | 0.26 | 1.19 | 0.13 | 0.476 | 0.039 | 0.136 | 0.010 |
| 80 | 3.94 | 0.44 | 1.30 | 0.13 | 0.539 | 0.045 | 0.177 | 0.011 |
| 90 | 3.09 | 0.51 | 1.48 | 0.23 | 0.474 | 0.02 | 0.227 | 0.023 |
| 100 | 2.00 | 0.26 | 1.19 | 0.22 | 0.313 | 0.035 | 0.182 | 0.019 |
| 110 | 2.43 | 0.37 | 1.10 | 0.26 | 0.356 | 0.027 | 0.162 | 0.013 |
| 120 | 3.63 | 0.33 | 1.26 | 0.18 | 0.456 | 0.037 | 0.158 | 0.011 |

| (d) $\theta$ (deg) | $r$ | Error | $r'$ | Error | $r''$ | Error | $r'''$ | Error |
|---|---|---|---|---|---|---|---|---|
| 20 | 3.34 | 0.22 | 2.46 | 0.22 | 0.241 | 0.038 | 0.222 | 0.023 |
| 25 | 3.46 | 0.23 | 2.26 | 0.21 | 0.331 | 0.044 | 0.228 | 0.024 |
| 30 | 3.28 | 0.22 | 2.13 | 0.19 | 0.339 | 0.041 | 0.221 | 0.023 |
| 35 | 3.73 | 0.23 | 2.16 | 0.20 | 0.283 | 0.027 | 0.164 | 0.016 |
| 40 | 3.35 | 0.20 | 2.10 | 0.17 | 0.233 | 0.022 | 0.147 | 0.015 |
| 45 | 3.30 | 0.21 | 1.84 | 0.15 | 0.192 | 0.021 | 0.108 | 0.011 |
| 50 | 3.02 | 0.22 | 1.57 | 0.16 | 0.166 | 0.018 | 0.087 | 0.009 |

TABLE III. (*Continued*.)

| | | | | | | | | |
|---|---|---|---|---|---|---|---|---|
| 60 | 2.22 | 0.15 | 1.19 | 0.12 | 0.166 | 0.012 | 0.089 | 0.009 |
| 70 | 1.72 | 0.12 | 0.965 | 0.080 | 0.219 | 0.018 | 0.123 | 0.013 |
| 80 | 1.75 | 0.12 | 0.995 | 0.078 | 0.298 | 0.024 | 0.169 | 0.017 |
| 90 | 1.62 | 0.12 | 0.975 | 0.077 | 0.316 | 0.025 | 0.191 | 0.020 |
| 100 | 1.52 | 0.11 | 0.802 | 0.059 | 0.304 | 0.019 | 0.160 | 0.017 |
| 110 | 1.60 | 0.11 | 0.653 | 0.043 | 0.355 | 0.019 | 0.123 | 0.013 |
| 120 | 2.12 | 0.13 | 0.561 | 0.051 | 0.480 | 0.026 | 0.127 | 0.013 |
| (e) $\theta$ (deg) | $r$ | Error | $r'$ | Error | $r''$ | Error | $r'''$ | Error |
| 15 | 2.51 | 0.35 | 2.92 | 0.34 | 0.048 | 0.024 | 0.042 | 0.020 |
| 20 | 2.23 | 0.32 | 2.57 | 0.31 | 0.087 | 0.010 | 0.101 | 0.012 |
| 25 | 2.73 | 0.38 | 2.38 | 0.28 | 0.148 | 0.017 | 0.130 | 0.016 |
| 30 | 2.41 | 0.35 | 2.00 | 0.24 | 0.176 | 0.021 | 0.146 | 0.018 |
| 35 | 2.77 | 0.40 | 1.84 | 0.22 | 0.182 | 0.021 | 0.121 | 0.015 |
| 40 | 2.84 | 0.45 | 1.77 | 0.23 | 0.177 | 0.023 | 0.110 | 0.015 |
| 45 | 2.93 | 0.43 | 1.67 | 0.20 | 0.168 | 0.020 | 0.096 | 0.012 |
| 50 | 2.78 | 0.38 | 1.53 | 0.18 | 0.171 | 0.019 | 0.094 | 0.011 |
| 60 | 2.52 | 0.37 | 1.26 | 0.15 | 0.144 | 0.017 | 0.073 | 0.009 |
| 70 | 1.70 | 0.25 | 1.06 | 0.13 | 0.163 | 0.020 | 0.105 | 0.013 |
| 80 | 1.53 | 0.22 | 0.961 | 0.117 | 0.216 | 0.026 | 0.150 | 0.019 |
| 90 | 1.30 | 0.19 | 0.972 | 0.118 | 0.257 | 0.030 | 0.193 | 0.024 |
| 95 | 1.29 | 0.19 | 1.01 | 0.13 | 0.268 | 0.033 | 0.211 | 0.027 |
| 100 | 1.75 | 0.28 | 0.914 | 0.121 | 0.324 | 0.042 | 0.174 | 0.024 |
| 110 | 2.02 | 0.33 | 0.746 | 0.101 | 0.418 | 0.056 | 0.154 | 0.022 |
| 120 | 3.02 | 0.49 | 0.670 | 0.090 | 0.559 | 0.073 | 0.125 | 0.017 |
| (f) $\theta$ (deg) | $r$ | Error | $r'$ | Error | $r''$ | Error | $r'''$ | Error |
| 10 | 2.02 | 0.20 | 2.27 | 0.22 | 0.008 | 0.001 | 0.033 | 0.014 |
| 15 | 1.97 | 0.19 | 2.13 | 0.21 | 0.060 | 0.007 | 0.065 | 0.008 |
| 20 | 2.18 | 0.22 | 1.91 | 0.20 | 0.105 | 0.011 | 0.089 | 0.009 |
| 25 | 2.06 | 0.24 | 1.71 | 0.20 | 0.122 | 0.014 | 0.103 | 0.012 |
| 30 | 1.89 | 0.20 | 1.60 | 0.17 | 0.093 | 0.010 | 0.110 | 0.012 |
| 35 | 1.83 | 0.19 | 1.46 | 0.16 | 0.121 | 0.013 | 0.103 | 0.011 |
| 40 | 1.84 | 0.20 | 1.41 | 0.15 | 0.125 | 0.013 | 0.098 | 0.011 |
| 45 | 1.79 | 0.20 | 1.37 | 0.15 | 0.126 | 0.014 | 0.103 | 0.011 |
| 50 | 1.95 | 0.21 | 1.27 | 0.14 | 0.132 | 0.014 | 0.093 | 0.010 |
| 60 | 2.01 | 0.22 | 1.15 | 0.13 | 0.155 | 0.017 | 0.094 | 0.010 |
| 70 | 2.24 | 0.26 | 1.06 | 0.12 | 0.187 | 0.022 | 0.088 | 0.010 |
| 80 | 1.54 | 0.16 | 0.958 | 0.102 | 0.211 | 0.022 | 0.121 | 0.013 |
| 90 | 1.08 | 0.13 | 0.947 | 0.110 | 0.192 | 0.022 | 0.149 | 0.017 |
| 100 | 1.22 | 0.14 | 0.900 | 0.106 | 0.235 | 0.028 | 0.159 | 0.019 |
| 110 | 2.08 | 0.25 | 0.852 | 0.101 | 0.355 | 0.043 | 0.144 | 0.018 |
| 120 | 3.29 | 0.40 | 0.833 | 0.101 | 0.502 | 0.062 | 0.130 | 0.019 |

lower than the present and Ref. [42] values, and they are in severe disagreement with the DBSR predictions.

Whereas level 1 (the $6s[3/2]_2$ state) is well *LS* coupled with a 0.996 amplitude due to the $5p^5 6s\ ^3P_2$ *LS*-coupled state, Table I shows that level 3 (the $6s'[3/2]_0$ state) is contaminated by the $5p^5 5d\ ^3P_0$ *LS* component with an amplitude of 0.413 (i.e., about a 17% contribution after squaring the coefficients) in the intermediate-coupling scheme. Hence, unlike in Ne and Ar, where both of these two states are well *LS* coupled and dominated by a single configuration, the $r$ parameter for Xe is expected to deviate from the statistical weight ratio of 5 as discussed in [36], either because of relativistic spin-orbit effects or due to an increased difference in $E_R$ as $E_0$ gets close to threshold. In [38] for Kr, oscillatory deviations of about 30% on average from the statistical weight value of $r = 5$ were observed for $E_0$ values of ≈3 eV above threshold. However, in Xe we see significantly reduced $r$ values below 5, i.e., values around 1–2, being observed at all $E_0$ values here. Theory does well to qualitatively reproduce these smaller $r$ values, but it needs to perform better quantitatively. We emphasize that the present data have smaller or comparable uncertainties than our earlier Xe measurements [23,42]. This is due to the better statistical counts in the present work that focused the data acquisition time only on the lowest four excited states of Xe, rather than on the extended spectrum of Xe studied in the previous work [23,24]. We also reckon that the lower values of $r$ at $E_0 = 20$ eV could be due to poorer statistics in their work with an extended spectrum.

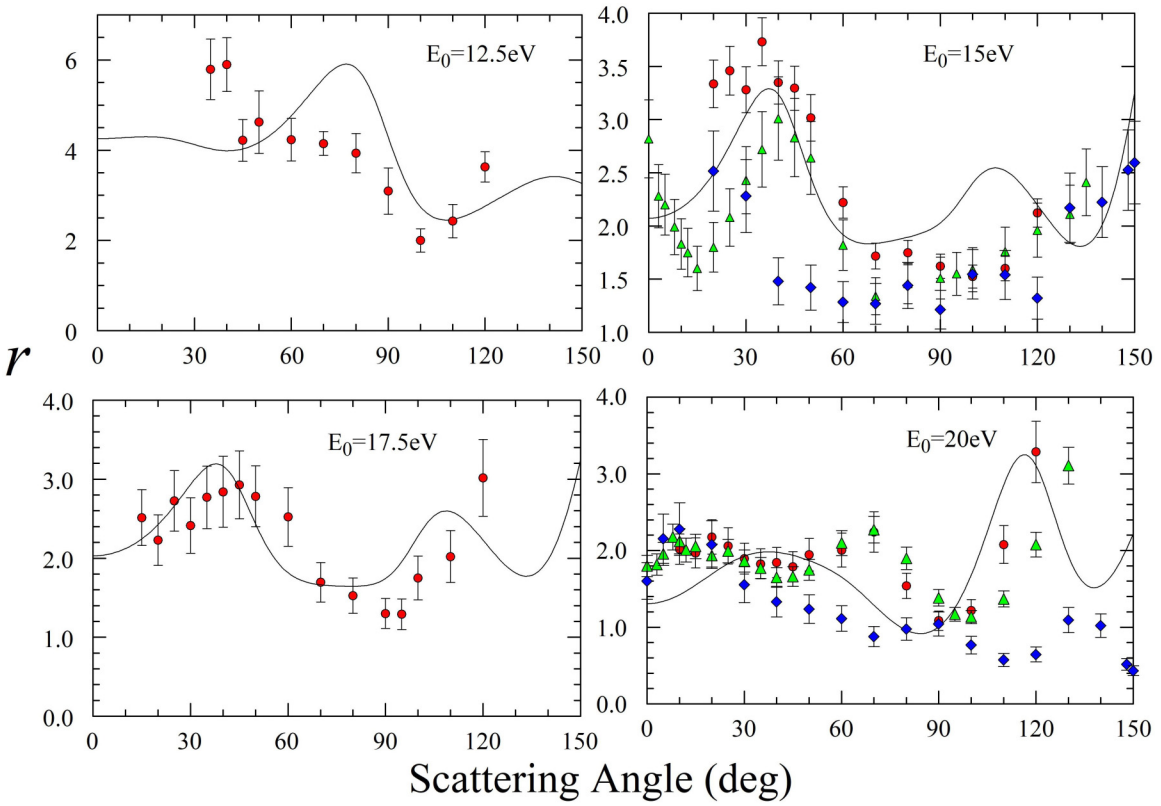


FIG. 2. Angle-differential $r$ values with associated errors taken at (a) $E_0 = 12.5$, 15.0, 17.5, and 20.0 eV. Experiments: (●) Present work; (▲) Khakoo *et al.* 1996 [23]; (♦) Filipović *et al.* 1988 [42]. Theory: DBSR-31 calculations. See text for discussion.

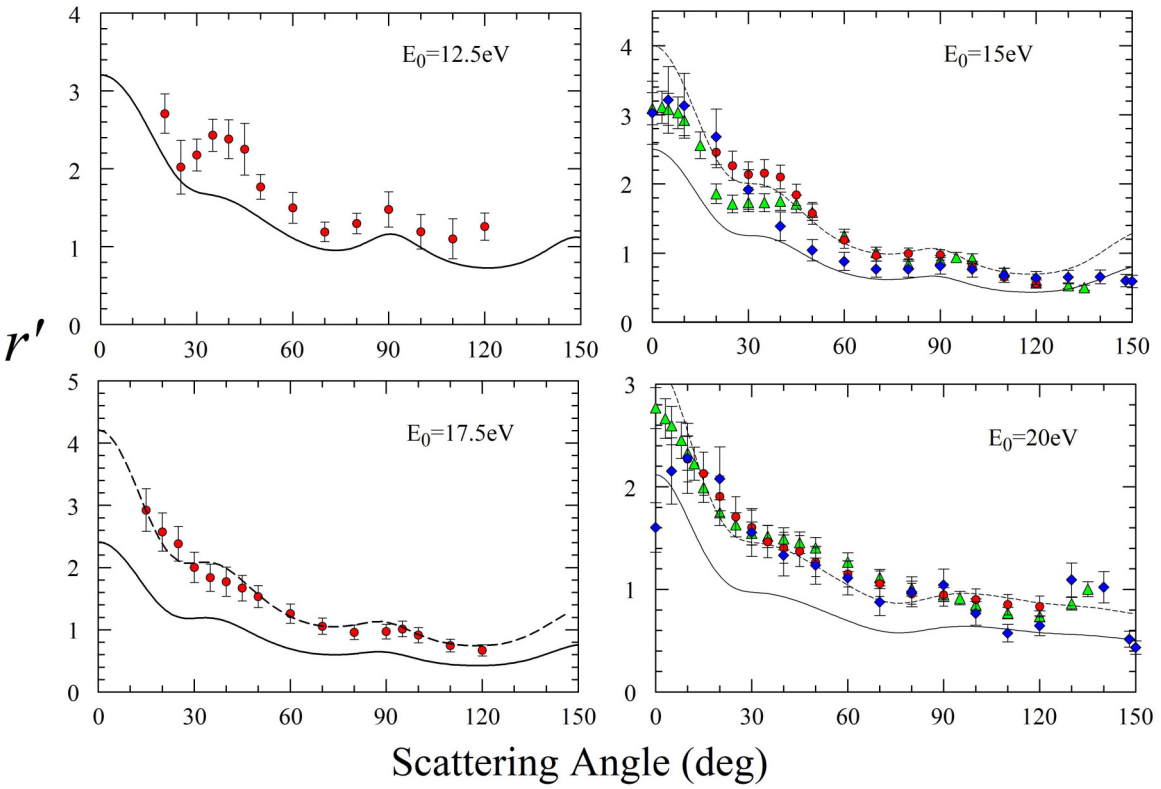


FIG. 3. Same as Fig. 2, but for the $r'$ ratios. The dashed lines represent the original DBSR-31 results multiplied by factors (see text) that visually improve the agreement with experiment. See text for a detailed discussion.

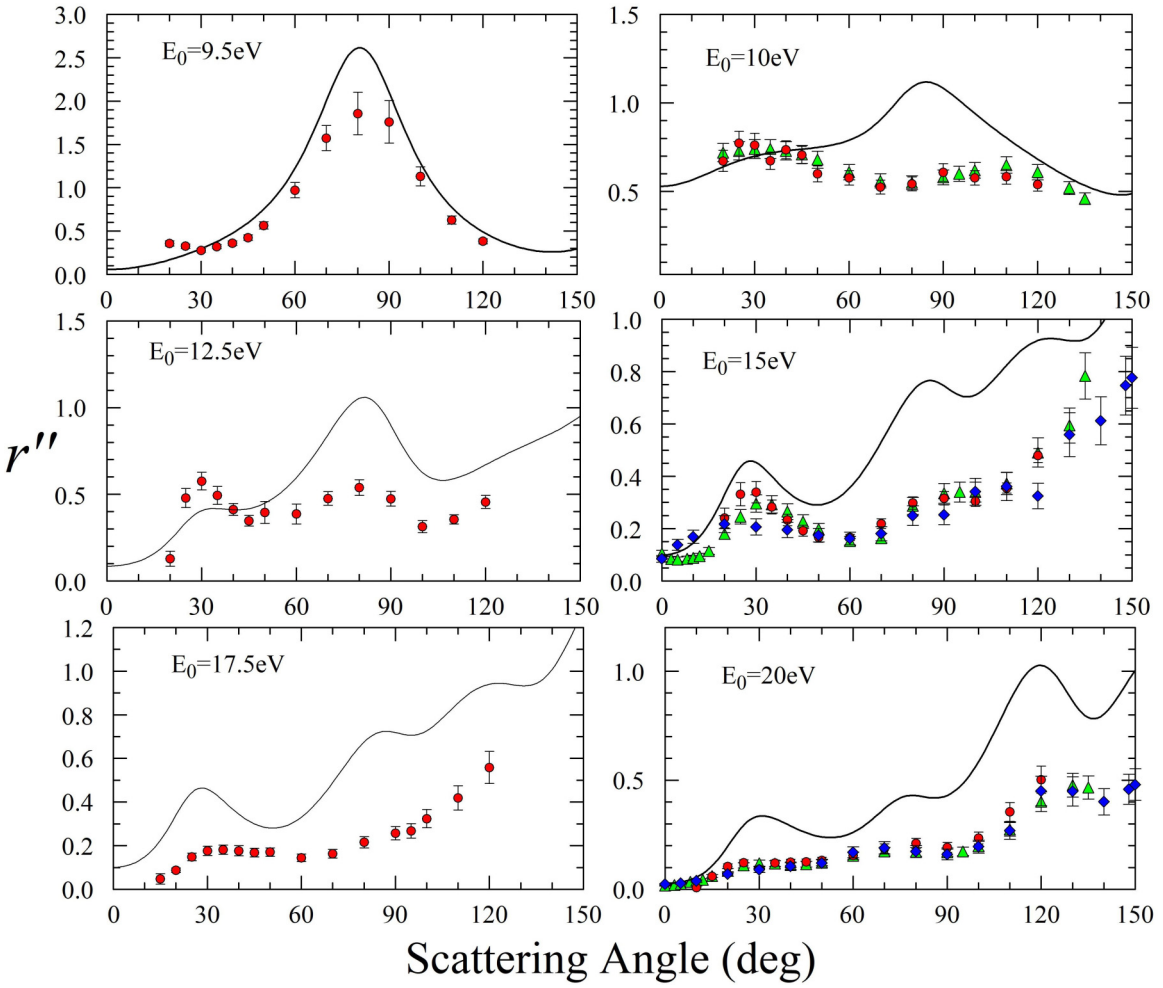


FIG. 4. Same as Fig. 2, but for the $r''$ ratios. See text for discussion.

In Fig. 3 for $r'$, we see generally excellent agreement between the measurements. For $E_0 = 15.0\,\text{eV}$, however, the present $r'$ values correct the earlier ones at $\theta \approx 30^\circ$ by about 30%. This yields an angular dependence that is better modeled qualitatively by the theory. However, the predictions have to be multiplied by a factor of ≈1.6 across the entire angular range for nearly perfect agreement with the experimental data. All experiments lie higher than theory, but the $r'$ values of [42] are closest to theory and could be due to a transmission increase in the spectrum from detecting feature 2 and detecting 4+5. A similar problem regarding the size of the $r'$ values is observed for $E_0 = 17.5\,\text{eV}$, where theory has to be multiplied by about 1.75 to better agree with the experimental data. At $E_0 = 20.0\,\text{eV}$, the two experimental datasets are in excellent agreement with each other within the estimated uncertainty of ≈11%. At this energy, the theoretical results should be multiplied by about 1.5 to get into good quantitative agreement with the measurements. Here transmission variation in the experiments is minimal, and we see all three experiments in very good agreement with each other. We note that these multiplication factors are only shown to provide a better visual comparison between experiment and theory in a qualitative sense. We do not presently understand the origin of this value, except that (again based on the very good agreement between the three experimental datasets) theory needs to be improved to remedy this.

In Fig. 4 we show results for the $r''$ ratio, which is our most accurate observable, since it is least affected by spectrometer transmission, i.e., <3% at $E_0$ of 9.5 eV and < 1% at higher $E_0$ values shown in Table II. This can be inferred from the excellent agreement for this ratio at all $E_0$ values. This ratio compares the $6s[3/2]_2$ state (which is very well $LS$ coupled; see Table I) to the $6s[3/2]_1$ state, which is also reasonably well represented within a single-configuration expansion in the intermediate-coupling scheme. Raised values of this parameter will very likely be linked to selective spin-exchange excitation of the triplet $LS$ components of both states, i.e., the $5p^5 6s\ ^3P_2$ for level 1 [numerator in $r'$] and the $5p^5 6s\ ^3P_1$ for level 2 [denominator in $r'$]. This also implies an inhibition in the direct singlet excitation of the $5p^5 6s\ ^1P_1$ $LS$ component of level 2. At $E_0 = 9.5\,\text{eV}$ we see enhanced spin exchange at $\theta = 80^\circ$, which is well reproduced by theory, except that experiment (1.86) is about 40% lower than theory (2.61), indicating reduced spin exchange. However, whereas the theoretical $r''$ ratio approaches zero at $\theta \to 0^\circ$, the experimental $r''$ ratio appears to differ significantly from that value. This is important, as it stresses significant spin-exchange processes are prevalent in Xe at small $\theta$. This was also observed in Kr

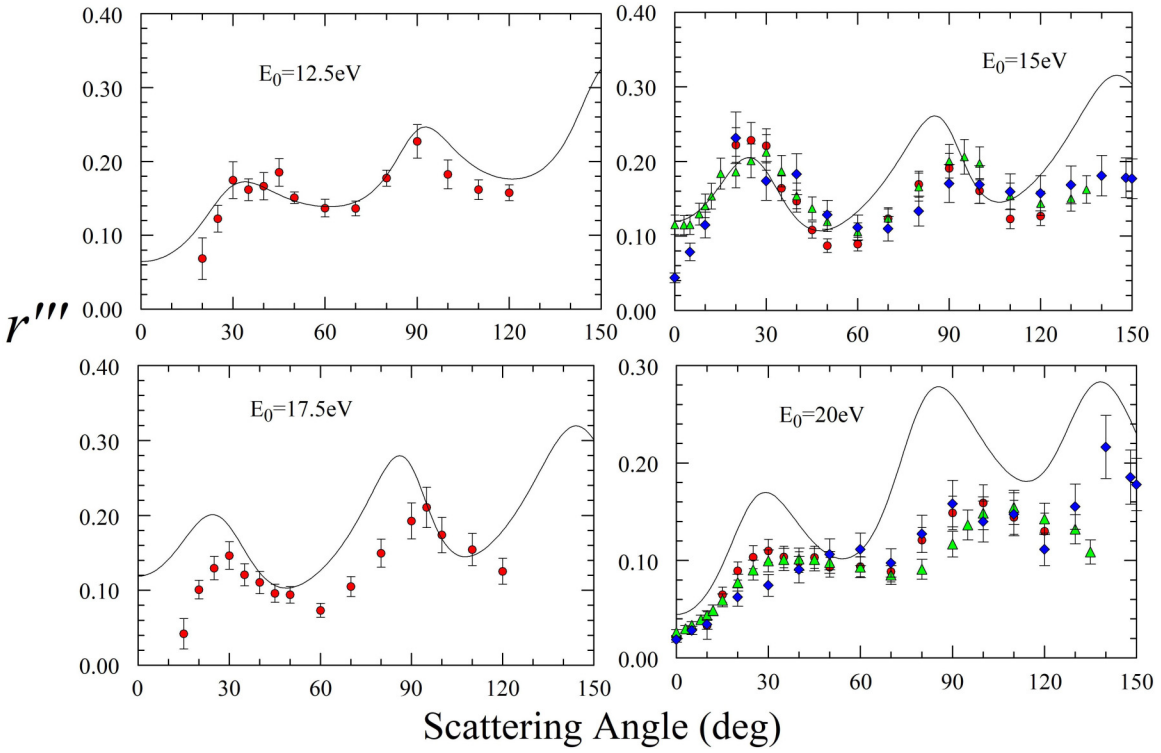


FIG. 5. Same as Fig. 2, but for the $r'''$ ratios. See text for discussion.

[38], where the $r''$ ratio at small $\theta$ was at clearly nonzero at all $E_0$ values. The presence of nonzero spin exchange for small $\theta$ might explain an "unusual" reversal in the observed orientation parameters in excitation of the Ne $(2p^6)\ ^1S_0 \rightarrow (2p^5 3s)\ [3/2]_1$ transition by electrons at $E_0 = 25$ eV at small $\theta$ reported by Hargreaves *et al.* [48]. For a pure singlet $\rightarrow$ singlet excitation by electron impact (direct process), it is well established that for a rare-gas $^1S_0 \rightarrow [3/2]_1\ ^1P_1$ excitation, the perpendicular angular momentum imparted to the excited state ($L_\perp$) at small $\theta$ should be positive [49]. In contrast, we found it to be anomalously negative for the resonance excitation of Ne at 25 eV. However, the Ne $(2p^5 3s)\ [3/2]_1$ state is a mixed singlet-triplet *LS* state with an intermediate-coupling expansion [11]:

$$(2p^5 3s)[3/2]_1 = 0.940(2p^5)3s\,^1P_1 + 0.340(2p^5)3s\,^3P_1. \quad (5)$$

Thus, it is possible to orient this state also with spin-angular momentum imparted through the spin-exchange process from the projectile to the target via an oriented spin-orbit coupling process in the target, and thereby to produce the negative $L_\perp$ value observed in [48]. Looking at Fig. 4, we see that the angular dependence of $r''$ changes considerably from $E_0 = 9.5$ eV to 10 eV. This is due to the role of resonances below the ionization of 12.13 eV and results in a complicated picture. See also the angle-integrated cross sections presented in [39]. Nevertheless, the earlier $r''$ measurements of [23] and the present ones are in excellent agreement with each other and are not systematically affected by these sharp resonances. Although our energy resolution is good, it is finite and hence will wash out some of these effects. In Xe the reduced spin exchange observed at small $\theta$, compared to that observed similarly in Kr [28], calls for further improvement of the DBSR model used so far. At the other $E_0$ values, we see improved qualitative agreement at $E_0$ values $\geqslant 15$ eV, but marked quantitative differences in some places (e.g., $E_0 = 15$ eV, $\theta \approx 90°$). We note that the experiments are found to be in excellent agreement with each other across the entire angular range to within 10% uncertainty. They reproduce the oscillatory nature of $r''$ very well, thereby suggesting this case as a suitable benchmark.

Figure 5 displays the $r'''$ parameter. Like $r''$ it contains (cf. Table I) a significant $6s'[1/2]_0 = 0.906\ (5p^5 6s^3P_0) + 0.413\ (5p^5 5d^3P_0)$ triplet excitation in the numerator. The agreement between all the three experiments is again excellent as was the case for $r''$, thus making this also a good benchmark ratio. We see similar oscillations in $r'''$ and $r''$. The $r'''$ error bars are larger than for $r''$ since the excitation of the $6s'[1/2]_0$ state (feature $m = 3$; see Fig. 1), which comprises this ratio, is the weakest among the levels 1–(4 + 5) in the Xe energy loss spectrum. At $E_0 = 12.5$ eV (all $\theta$ ) and $E_0 = 15$ eV ($\theta \leqslant 50°$) excellent (quantitative) agreement between experiment and theory is observed. Elsewhere, the agreement is qualitatively good. Here theory reproduces the peaks for $\theta \approx 30°$ and 90 ° in $r'''$ at all $E_0$ values. If one assumes that the higher $r'''$ values imply increased spin-exchange processes, we observe spin exchange for all $\theta$, including near-forward scattering angles.

## VI. CONCLUSIONS

We have presented recent measurements of intensity ratios $r$, $r'$, $r''$, and an additional useful ratio $r'''$, for electron-impact excitation of the lowest five excited states of Xe as was done earlier for Kr [38]. These were compared with earlier Xe ratios taken in our laboratory [23] and with DBSR calculations for

*e*-Xe collisions. The agreement between the present measurements and earlier [23,42] data is very good for $r$ and $r'$ and excellent for $r''$ and $r'''$. This provides confidence in the overall reliability of the experimental data.

Unfortunately, the overall agreement of the experimental ratios with the theoretical predictions is not as good as it was for Kr, and both Ref. [38] and the present work make suggestions where the DBSR model may need to be improved even further. There is an important motivation for improving the DBSR theory for electron scattering from multielectron atomic targets, so that it can be used to model electron-collision problems with other, even more complex many-electron targets. New calculations with a further improved target structure and even more coupled states in the collision part of the problem seem necessary to achieve the needed progress. Unfortunately, such calculations require enormous computational effort and cannot be carried out at this time with our available resources.

We hope that progress in computer power and software will make this feasible. We also hope that the present work on Xe, and [38] on Kr, will provide an impetus for theory to further push benchmark calculations for electron scattering from multielectron targets with more than two electrons outside of a structureless core by employing the close-coupling formalism.

## ACKNOWLEDGMENTS

This work was funded by the U.S. National Science Foundation to M.A.K. under Grants No. NSF-RUI AMO 106905 and No. 1911702 which funded A.S.'s Postdoctoral Fellowship. The work of O.Z. and K.B. was supported by the NSF under Grants No. PHY-1803844, No. OAC-1834740, and No. PHY-2110023, and by the XSEDE Allocation No. TG-PHY-090031.

[1] M. Wendt, S. Peters, D. Loffhagen, A. Kloss, and M. Kettlitz, J. Phys. D: Appl. Phys. **42**, 185208 (2009).
[2] B. W. Hodgson and J. P. Keene, Rev. Sci. Instrum. **43**, 493 (1972).
[3] J. P. Boeuf, J. Phys. D: Appl. Phys. **36**, R53 (2003).
[4] P. D. Harris and R. Barnes, Anaesthesia **63**, 284 (2008).
[5] J. P. Mugler III, T. A. Altesa, I. C. Ruset, I. M. Dregely, J. F. Mata, G. W. Miller, S. Ketel, J. Ketel, F. W. Hersman, and K. Ruppert, Proc. Natl Acad. Sci. USA **107**, 21707 (2010).
[6] K. Bartschat and D. H. Madison, J. Phys. B: At. Mol. Phys. **20**, 5839 (1987).
[7] J. B. Furness and I. E. McCarthy, J. Phys. B: At. Mol. Phys. **6**, 2280 (1973).
[8] M. A. Khakoo and J. W. McConkey, J. Phys. B At. Mol. Phys. **20**, 5541 (1987).
[9] T. Zuo, R. P. McEachran, and R. P. Stauffer, J. Phys. B: At. Mol. Phys. **25**, 3393 (1992).
[10] R. D. Cowan, *The Theory of Atomic Structure and Spectra* (University of California Academic Press, Riverside, CA, 1981).
[11] M. A. Khakoo, J. Wrkich, M. Larsen, G. Kleiban, I. Kanik, S. Trajmar, M. J. Brunger, P. J. O. Teubner, A. Crowe, C. J. Fontes, R. E. H. Clark, V. Zeman, K. Bartschat, D. H. Madison, R. Srivastava, and A. D. Stauffer, Phys. Rev. A **65**, 062711 (2002).
[12] I. Bray and A. T. Stelbovics, Phys. Rev. A **46**, 6995 (1992).
[13] D. V. Fursa and I. Bray, Phys. Rev. A **52**, 1279 (1995).
[14] K. Bartschat, E. T. Hudson, M. P. Scott, P. G. Burke, and V. M. Burke, J. Phys. B: At. Mol. Phys. **29**, 115 (1996).
[15] E. T. Hudson, K. Bartschat, M. P. Scott, P. G. Burke, and V. M. Burke, J. Phys. B: At., Mol. Opt. Phys. **29**, 5513 (1996).
[16] M. C. Zammit, J. S. Savage, D. V. Fursa, and I. Bray, Phys. Rev. Lett. **116**, 233201 (2016).
[17] K. Bartschat and I. Bray, J. Phys. B: At., Mol. Opt. Phys. **29**, L577 (1996).
[18] D. V. Fursa and I. Bray, J. Phys. B: At., Mol. Opt. Phys. **30**, 757 (1997).
[19] M. C. Zammit, J. S. Savage, D. V. Fursa, and I. Bray, Phys. Rev. A **95**, 022708 (2017).
[20] R. Poet, J. Phys. B: At. Mol. Phys. **11**, 3081 (1978).
[21] K. A. Berrington, P. G. Burke, J. J. Chang, A. T. Chivers, W. D. Robb, and K. T. Taylor, Comput. Phys. **8**, 149 (1974).
[22] N. S. Scott and P. G. Burke, J. Phys. B: At. Mol. Phys. **13**, 4299 (1980).
[23] M. A. Khakoo, S. Trajmar, L. R. LeClair, I. Kanik, G. Csanak, and C. J. Fontes, J. Phys. B: At., Mol. Opt. Phys. **29**, 3455 (1996).
[24] M. A. Khakoo, S. Trajmar, S. Wang, I. Kanik, A. Aguirre, C. J. Fontes, R. E. H. Clark, and J. Abdallah, J. Phys. B: At., Mol. Opt. Phys. **29**, 3477 (1996).
[25] X. Guo, D. F. Mathews, G. Mikaelian, M. A. Khakoo, A. Crowe, I. Kanik, S. Trajmar, V. Zeman, K. Bartschat, and C. J. Fontes, J. Phys. B: At., Mol. Opt. Phys. **33**, 1895 (2000).
[26] X. Guo, D. F. Mathews, G. Mikaelian, M. A. Khakoo, A. Crowe, I. Kanik, S. Trajmar, V. Zeman, K. Bartschat, and C. J. Fontes, J. Phys. B: At., Mol. Opt. Phys. **33**, 1921 (2000).
[27] O. Zatsarinny, Comput. Phys. Commun. **174**, 273 (2006).
[28] O. Zatsarinny and K. Bartschat, J. Phys. Conf. Ser. **488**, 012044 (2014).
[29] O. Zatsarinny and K. Bartschat, Phys. Rev. A **77**, 062701 (2008).
[30] Oleg Zatsarinny's GitHub Repository. Available online: https://github.com/zatsaroi.
[31] Atomic, Molecular, and Optical Science Gateway, online: https://amosgateway.org/.
[32] O. Zatsarinny, Y. Wang, and K. Bartschat, Phys. Rev. A **89**, 022706 (2014).
[33] M. J. Brunger and S. J. Buckman, Phys. Rep. **357**, 215 (2002).
[34] M. Zawadzki, R. Wright, G. Dolmat, M. F. Martin, L. Hargreaves, D. V. Fursa, M. C. Zammit, L. H. Scarlett, J. K. Tapley, J. S. Savage, I. Bray, and M. A. Khakoo, Phys. Rev. A **97**, 050702(R) (2018).
[35] J. Muse, H. Silva, M. C. A. Lopes, and M. A. Khakoo, J. Phys. B: At., Mol. Opt. Phys. **41**, 095203 (2008).

[36] K. Bartschat and D. H. Madison, J. Phys. B: At., Mol. Opt. Phys. **25**, 4619 (1992).
[37] O. Zatsarinny and K. Bartschat, Phys. Rev. A **86**, 022717 (2012).
[38] A. Sakaamini, J-B. Faure, M. A. Khakoo, O. I. Zatsarinny, and K. Bartschat, Atoms **9**, 61 (2021).
[39] O. Zatsarinny and K. Bartschat, J. Phys. B: At., Mol. Opt. Phys. **43**, 074031 (2010).
[40] C. J. Fontes, Los Alamos National Laboratory, Los Alamos, NM (private communication), 1996.
[41] C. E. Moore, *Atomic Energy Levels*, NSRDS-NBS 35 (National Bureau of Standards, U.S. Government Publishing, Washington, DC, 1957), Vol. 35.
[42] D. Filipović, B. Marinković, V. Pejčev, and L. Vušković, Phys. Rev. A **37**, 356 (1988).
[43] P. Jönsson, X. He, C. Froese Fischer, and I. P. Grant, Comput. Phys. Commun. **177**, 597 (2007).
[44] M. A. Khakoo, C. E. Beckmann, S. Trajmar, and G. Csanak, J. Phys. B: At., Mol. Opt. Phys. **27**, 3159 (1994).
[45] J. H. Brunt, G. C. King, and F. H. Read, J. Phys. B: At., Mol. Phys. **10**, 1289 (1977).
[46] A. Gopalan, J. Bömmels, S. Götte, A. Landwehr, K. Franz, M. W. Ruf, H. Hotop, and K. Bartschat, Eur. Phys. J. D **22**, 17 (2002).
[47] M. A. Khakoo, K. Keane, C. Campbell, N. Guzman, and K. Hazlett, J. Phys. B: At., Mol. Opt. Phys. **40**, 3601 (2007).
[48] L. R. Hargreaves, C. Campbell, M. A. Khakoo, O. Zatsarinny, and K. Bartschat, Phys. Rev. A **85**, 050701(R) (2012).
[49] L. R. Hargreaves, R. Wright, M. A. Khakoo, O. Zatsarinny, K. Bartschat, Dipti, R. Srivastava, and A. D. Stauffer, J. Phys. B: At., Mol. Opt. Phys. **48**, 185201 (2015).